Biomaterials Translational

Abalone shell-derived Mg-doped mesoporous hydroxyapatite microsphere drug delivery system loaded with icariin for inducing apoptosis of osteosarcoma cells

Kaihua Liu[1,2,#], Meiqi Cheng[1,#], Hao Huang[3], Hui Yu[1], Shiyao Zhao[1], Jinnuo Zhou[1], Dan Tie[1], Jianhua Wang[3], Panpan Pan[1,], Jingdi Chen[1,2,*]*

Key Words:
abalone shell; drug delivery; hydroxyapatite microspheres; magnesium doping; osteosarcoma

From the Contents

ABSTRACT

Hydroxyapatite (HAP) porous microspheres with very high specific surface area and drug loading capacity, as well as excellent biocompatibility, have been widely used in tumour therapy. Mg^{2+} is considered to be a key factor in bone regeneration, acting as an active agent to stimulate bone and cartilage formation, and is effective in accelerating cell migration and promoting angiogenesis, which is essential for bone tissue repair, anti-cancer, and anti-infection. In this study, abalone shells from a variety of sources were used as raw materials, and Mg^{2+}-doped abalone shell-derived mesoporous HAP microspheres (Mg-HAP) were prepared by hydrothermal synthesis as Mg^{2+}/icariin smart dual delivery system (ICA-Mg-HAP, IMHA). With increasing of Mg^{2+} doping, the surface morphology of HAP microspheres varied from collapsed macroporous to mesoporous to smooth and non-porous, which may be due to Mg^{2+} substitution or coordination in the HAP lattice. At 30% Mg^{2+} doping, the Mg-HAP microspheres showed a more homogeneous mesoporous morphology with a high specific surface area (186.06 m^2/g). The IMHA microspheres showed high drug loading (7.69%) and encapsulation rate (83.29%), sustained Mg^{2+} release for more than 27 days, sustained and stable release of icariin for 60 hours, and good responsiveness to pH (pH 6.4 > pH 5.6). In addition, the IMHA delivery system stimulated the rapid proliferation of bone marrow mesenchymal stem cells and induced apoptosis in MG63 cells by blocking the G2 phase cycle of osteosarcoma cells and stimulating the high expression of apoptotic genes (Bcl-2, caspase-3, -8, -9). This suggests that the abalone shell-based IMHA may have potential applications in drug delivery and tumour therapy.

http://doi.org/10.12336/biomatertransl.2024.02.008

How to cite this article:
Liu, K.; Cheng, M.; Huang, H.; Yu, H.; Zhao, S.; Zhou, J.; Tie, D.; Wang, J.; Pan, P.; Chen, J. Abalone shell-derived Mg-doped mesoporous hydroxyapatite microsphere drug delivery system loaded with icariin for inducing apoptosis of osteosarcoma cells. *Biomater Transl.* **2024**, *5*(2), 185-196.

Introduction

Hydroxyapatite (HAP), as the major inorganic component of vertebrate bone, is a biodegradable bioactive material with good biocompatibility, excellent osseointegration, and osteoconductivity, and is widely applied for bone tissue regeneration.[1-3] Industrial synthetic HAP is commonly prepared by hydrothermal synthesis using calcium phosphate or calcium nitrate as calcium sources. Interestingly, the abalone shell is rich in calcium carbonate (> 95%) and small amounts of functional trace elements (e.g., magnesium (Mg), iron (Fe), copper (Cu), etc.), which is expected to provide a rich material source for HAP,[4-6] and at the same time realise the high-value utilisation of discarded abalone shell resources to solve the problems of environmental pollution and resource waste. However, the function of pure HAP is relatively simple, and the exploration of structural modification and functional features of HAP needs further breakthroughs.

To date, HAP has been successfully prepared in various morphologies, such as spherical, needle,

flower, and rod.[7-10] Among them, spherical mesoporous HAP has important structural advantages in drug delivery and tumour treatment because of its unique mesoporous channels, large specific surface area, good biocompatibility, and degradation characteristics with pH value.[11-13] In addition, by doping or substituting HAP with functional ion,[14, 15] additional functional properties (e.g., targeting,[16, 17] anti-microbial properties)[18-20] can be imparted to meet the needs of specific applications. The release of Mg^{2+} from HAP after the doping of metallic Mg in HAP could significantly improve the osteoinductivity of HAP, and thus promote osteogenic differentiation.[21] Mg^{2+} is widely used in cancer therapy, where it can be effective as a common immunomodulator and is essential for the immune system to fight against cancer and infection.[22, 23] However, the reported functionally doped HAP are mostly monomorphic structures such as needle flakes,[24, 25] which are not sufficient for application in biopharmaceutical carriers. Designing the functionally doped/modified HAP into a three-dimensional mesoporous structure is expected to overcome this challenge.

In this study, Mg^{2+}-doped icariin-loaded HAP mesoporous microspheres (IMHA) were prepared by hydrothermal synthesis using abalone shell as the calcium source to achieve the intelligent dual delivery of Mg^{2+} and ICA. The sodium citrate template agent ionises three carboxyl groups, which could simultaneously chelate Ca^{2+} and Mg^{2+} in solution. Then, it exists as nucleation sites during the hydrothermal process, adsorbs OH^- and PO_4^{3-} in solution, and crystallises oriented self-assembly to form MHA mesoporous microspheres (**Figure 1**). By the spherical mesoporous structure and high phase purity of MHA, a large amount of OH^- can be provided for hydrogen bonding interactions with the drug ICA, resulting in high drug loading. The conformational relationship between the doping amount of Mg^{2+} and the morphological structure and function of microspheres was investigated, revealing the drug loading and release patterns of the microspheres. Finally, the biocompatibility, anti-tumour properties, and mechanism of action of microspheres before and after drug loading were elucidated.

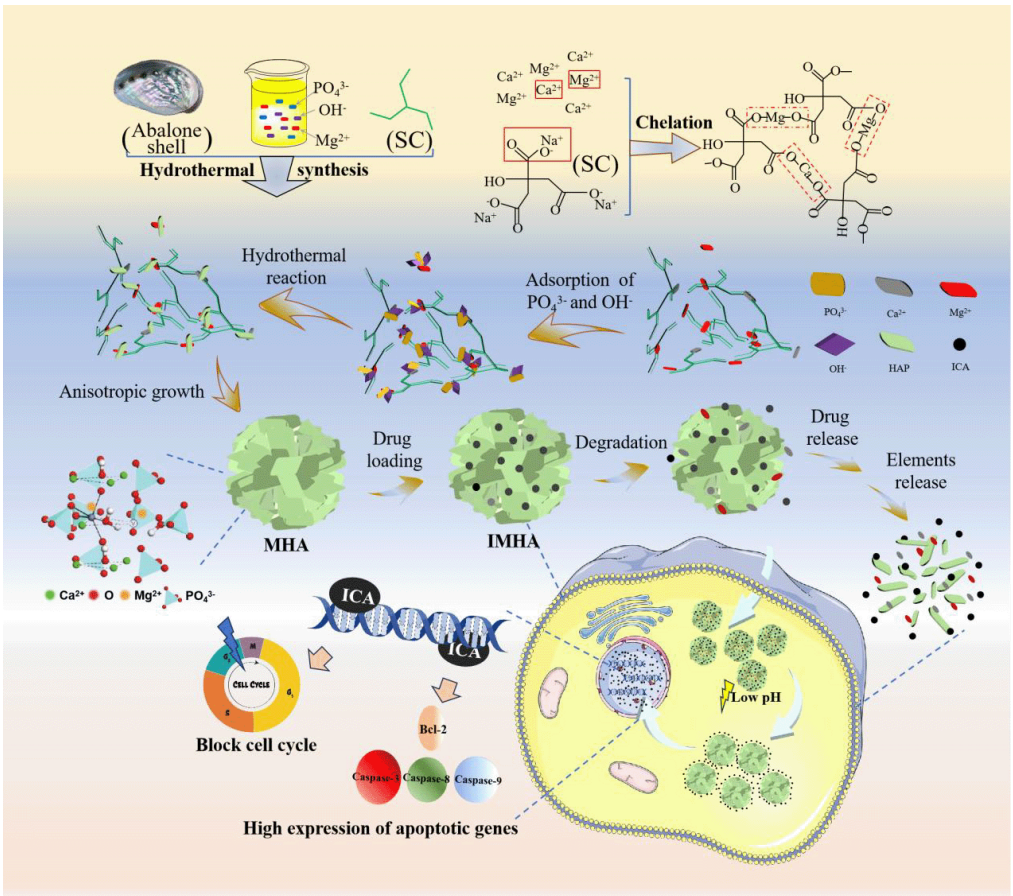

Figure 1. Schematic representation of the synthesis and release of Mg^{2+}-doped icariin-loaded hydroxyapatite mesoporous microspheres. ICA: icariin; IMHA: Mg^{2+}/icariin smart dual delivery system; MHA: Mg^{2+}-doped abalone shell-derived mesoporous hydroxyapatite microspheres; SC: sodium citrate.

1 Marine College, Shandong University, Weihai, Shandong Province, China; 2 State Key Laboratory of Mineral Processing, Beijing, China; 3 College of Biological Science and Technology, Fuzhou University, Fuzhou, Fujian Province, China

***Corresponding authors:** Jingdi Chen, jdchen@sdu.edu.cn; Panpan Pan, pppan@sdu.edu.cn.

#Author equally.

Methods

Synthesis of Mg-doped hydroxyapatite microspheres

Abalone shells (Dockyard Ocean Development Co., Ltd., Fuzhou, China). were processed according to our previous method[5] to obtain abalone shell powder. A certain amount of abalone shell powder was weighed into the beaker, and 20 mL acetic acid solution (10 vol%, CH_3COOH, 99.5%, Shanghai MacLean Biochemical Co., Ltd., Shanghai, China) was added to dissolve the abalone shell powder. The mixture was stirred continuously until no bubbles were formed. Water was added to the supernatant obtained after centrifuging the mixture to a volume of 50 mL, and then 50 mL phosphoric acid (H_3PO_4, 85%, 0.06 M, 1 mL/min, Shanghai MacLean Biochemical Co., Ltd.) was added slowly while stirring. Subsequently, magnesium chloride ($MgCl_2{\cdot}6H_2O$, Shanghai MacLean Biochemical Co., Ltd.), sodium citrate (10 mL, 0.08 M, Shanghai MacLean Biochemical Co., Ltd.), and $CO(NH_2)_2$, 6 g, Shanghai MacLean Biochemical Co., Ltd.) were added to the solution and stirred continuously for 0.5 hour until the precursor solution was clear. The additional amounts of $MgCl_2{\cdot}6H_2O$ and abalone shell powder were adjusted to ensure a molar ratio of (Ca + Mg) to P of 1.67 (**Additional Table 1**). After stirring, the precursor solution was poured into the reaction kettle. Hydrothermal reaction was carried out under high pressure at 90°C for 40 hours. Finally, the mesoporous microspheres of Mg-doped HAP (Mg-HAP, donated as MHA) were obtained by cooling to room temperature, washing by centrifugation three times (9000 r/min, 5 minutes), washing once with ethanol (Shanghai MacLean Biochemical Co., Ltd.), and drying at 60°C. When the addition of Mg^{2+} is 0%, the prepared MHA is named MHA0, or M0 for short. Similarly, when the addition of Mg^{2+} ($Mg^{2+}/(Mg^{2+} + Ca^{2+}) \times 100\%$) is 10%, 20%, 30%, 40%, and 50% respectively, the samples are named M10, M20, M30, M40, and M50, respectively. It should be noted that the components and experimental conditions of M0–50 are the same except for the different amounts of Mg^{2+} and Ca^{2+}.

Synthesis of ICA-loaded MHA microspheres

50 mg of MHA was added to 5 mL of ICA solution (1 mg/mL, Xi'an Realin Biotechnology Co., Ltd., Xi'an, China), and continuously shaken at 37°C for 48 hours in a constant temperature shock incubator. The mixed suspension was then centrifuged and washed three times. The precipitate was dried in a vacuum at 60°C and protected from light to obtain ICA-loaded Mg-HAP microspheres (donated as IMHA).

Characterisation

It was analysed by solid phase X-ray diffraction, field emission scanning electron microscopy, transmission electron microscopy, Fourier transform infrared spectrometer and Renishaw invia Raman microscope. Inductively coupled plasma, Asap2460 analyser (Atlanta, GA, USA) and enzyme labeling instrument were used for the test.[26, 27] The details are shown in **Additional file 1**.

Element releasing analysis

0.1 g of MHA was immersed in phosphate buffered solution (PBS) with a water bath at 37°C. Over the next 28 days, 1 mL of solution was collected to monitor the changes in the contents of Ca, Mg, and P elements, and fresh PBS was added at the regular intervals.[5]

Haemolysis performance analysis

All animal experiments in this study followed the Ethical Guidelines for the Management and Welfare of Animal Experiments at Shandong University (No. 20231012). A 2.5% sodium pentobarbital solution was prepared, and New Zealand white rabbits (Jinan Xilingjiao Breeding Center, License No. SCXK (Lu) 2024-0001) were anaesthetised by intravenous injection (1.5 mL/kg) at the ear margin. Venous blood was collected with a syringe from the ears of anaesthetised New Zealand white rabbits (n = 6, 8 months old, male) and quickly added to the centrifuge tube with heparin solution infiltrated into the inner wall and stirred gently, and quickly added to the centrifuge tube with heparin solution infiltrating the inner wall, and stir it slightly. Then the rabbit blood mixture was centrifuged 2–3 times (4500 r/min, 10 minutes, 37°C) to collect clean red blood cells, and then the collected red blood cells were diluted to 5% concentration with normal saline to obtain anti-coagulant rabbit blood, which is stored at 4°C for later use.

2 mL anti-coagulant rabbit blood, 2 mL normal saline, and different quality MHA were added into four test tubes (microspheres concentration gradients were 50, 100, 500, and 1000 μg/mL), respectively. Anti-coagulant rabbit blood (2 mL) was added to distilled water or normal saline as the positive and negative control groups of the experiment. The absorbance of 2 mL supernatant was measured at 545 nm by ultraviolet spectrophotometer (UV-2550, Xiamen Yichen Technology Co., Ltd., Xiamen, China). The haemolysis rate of MHA was calculated according to equation 1.[28, 29]

$$\text{Haemolysis (\%)} = (\text{optical density (OD)}_{\text{sample}} - \text{OD}_{\text{negative control}})/(\text{OD}_{\text{positive control}} - \text{OD}_{\text{negative control}}) \times 100 \quad (1)$$

Construction of ICA standard curve

Before measuring the drug loading and drug release of MHA, drug standard curve should be developed to calculate the drug loading capacity of microspheres. ICA was used as the sample drug in this experiment. The ICA solution was diluted to 10, 25, 50, and 100 μg/mL. The absorbance of the ICA solution was measured using an ultraviolet spectrophotometer (477 nm), and the ICA concentration-absorbance curve was plotted. The linear regression equation of the ICA standard curve was obtained by linear fitting (OriginPro 2024SR1), and the R-value reflected the degree of fit of the regression line to the observed values.

Drug carrying capacity evaluation

The absorbance of free ICA was measured by spectrophotometer (477 nm), and the ICA content in the supernatant was obtained by ICA standard curve. The encapsulation rate and drug load of IMHA were calculated according to equations 2 and 3, respectively.[5, 30]

$$\text{ICA entrapment efficiency (\%)} = (\text{ICA}_{\text{initial}} - \text{ICA}_{\text{in supernatant}})/(\text{ICA}_{\text{initial}}) \times 100 \quad (2)$$

ICA loading content (%) = ($ICA_{initial}$ – $ICA_{in\ supernatant}$)/(MHA_{amount}) × 100 (3)

Release behavior study of ICA

10 mg of IMHA was placed in a dialysis bag (8000–14,000 kDa, JIELEPU, Changsha, China) and placed in 30 mL PBS with pH at 7.4, 6.5, and 5.4, respectively while shaking in a shaking box (37°C, 150 r/min). Three parallel experiments were performed in each group. 2 mL of supernatant was withdrawn at each time for a specified period of time, and the concentration of ICA removed was measured at 477 nm, and the amount and rate of ICA release were calculated from the ICA standard curve. It was worth noting that the ICA contained in the removed PBS was also counted when calculating the cumulative drug release.

***In vitro* biocompatibility evaluation**

Generation 3 bone marrow mesenchymal stem cells (BMSCs) (Typical Culture Preservation Committee Cell Bank of the Chinese Academy of Sciences, Shanghai, China, Serial No. SCSP-402, STR: 19375.09.3101RATSCSP402) in good condition were selected, the medium was removed, trypsin was used to digested and added to complete culture medium to make cell suspension, counted and inoculated into sterile 96-well plates at 5×10^3 cells/well. After 24 hours of incubation in the cell culture incubator, different concentrations of MHA and IMHA were added and cultured in direct contact with BMSCs. After 1, 2, and 3 days of co-culture, Cell Counting Kit-8 (CCK-8) working solution (10 vol%, Sinopharm Group Ltd., Shanghai, China) was added to the well plates, and the OD at 450 nm of each well was measured rapidly after 3 hours of incubation in the cell culture incubator, and cell viability was calculated based on the OD values according to equation 4.[5]

Cell viability (%) = (OD_{sample} – OD_{blank})/($OD_{control}$ – OD_{blank}) × 100% (4)

***In vitro* anti-osteosarcoma performance**

MG63 osteosarcoma cells (Typical Culture Preservation Committee Cell Bank of the Chinese Academy of Sciences, Serial No. TCHu124, CSTR: 19375.09.3101HUMTCHu124, RRID: CVCL_0426) were cultured with different concentrations of MHA and IMHA, and then detected with CCK-8, acridine orange (AO)/ethidium bromide (EB) staining (Beijing Soleberg Technology Co., Beijing, China), cell cycle experiment (Shanghai BestBio, Shanghai, China) and Annexin V-fluorescein isothiocyanate (FITC) assay (Shanghai BestBio).[5]

CCK-8 assay

MG63 cells were selected to prepare cell suspension, counted, and inoculated into sterile 96-well plates at 5×10^3 cells/well. After 24 hours of incubation in the cell culture incubator, different concentrations of MHA and IMHA (50, 100, 500, and 1000 μg/mL) were added and further incubated in the incubator. After 1, 2, and 3 days of co-culture, CCK-8 working solution (10 vol%) was added to the well plates, and the OD at 450 nm of each well was rapidly measured after 3 hours of incubation in the cell culture incubator. The cell viability was calculated based on the OD values.

AO/EB staining assay

MG63 cells were cultured with different concentrations of MHA and IMHA (50, 100, 500, and 1000 μg/mL) for 48 hours. After 48 hours of incubation, AO/EB dual-colour fluorescent working solution (10 vol%) was added into the 24-well plates for 3–5 minutes, and washed twice with PBS, and then observed with an inverted fluorescence microscope (IX-71, Olympus Corporation, Beijing, China) under the condition of avoiding light.

Cell cycle assay

After co-culturing of different concentrations of IMHA (50, 100, 500, and 1000 μg/mL), MG63 cells were trypsin digested, PBS washed, and fixated at 4°C overnight in 75% frozen ethanol. After fixation, the cells were resuspended in cold PBS and RNase A solution was added to the cells in a 37°C water bath. The cells were mixed with the propidium iodide solution and incubated at 4°C for 30 minutes, protected from light, and then analysed by flow cytometry (FACSVerse, BD, Franklin Lakes, NJ, USA) within 24 hours.

Annexin V-FITC assay

MG63 cells were co-cultured with IMHA. Then, the cells were digested, washed, resuspended, and counted. 1×10^5 cells were stained with 500 μL of 1× binding buffer, 5 μL of Annexin V-FITC and 10 μL of propidium iodide staining solution, and the reaction was gently blown to mix well and avoided the light for 15 minutes, and then the reaction was carried out by flow cytometry within 1 hour.

Real-time polymerase chain reaction

MG63 cells were co-cultured with MHA and IMHA microspheres with different mass gradients. Total RNA of MG63 cells was extracted with Trizol reagent (Shanghai Inshore Protein Technology Co., Ltd., Shanghai, China). The RNA reverse transcription and reverse transcription-polymerase chain reaction (preheat 95°C for 1 minute; 35–45 cycles: 95°C for 20 seconds, 50–60°C for 20 seconds, 72°C for 30 seconds) were performed with first-chain reverse transcription kit (Shanghai Inshore Protein Technology Co., Ltd.) and fluorescence quantitative amplification kit (Shanghai Inshore Protein Technology Co., Ltd.). **Additional Table 2** lists the forward and reverse primer sequences of the apoptosis genes.[31, 32]

Statistical analysis

All data sets were analysed independently and are expressed as the mean ± standard deviation (SD). OriginPro 2024SR1 and IBM SPSS Statistics 24 software (IBM Corp., Armonk, NY, USA) were selected for data analysis. A one-way analysis of variance and least significant difference *post hoc* test were used to assess the statistical significance of the data. $P < 0.05$ was considered statistically significant.

Results

Physicochemical characterization of MHA and IMHA microspheres

Scanning electron microscope (SEM) images showed the

microscopic morphology of MHA with different doping levels of Mg^{2+} (**Figure 2A** and **Additional Figure 1**). When the Mg^{2+} was not doped, the prepared samples showed a spherical porous structure, but the crystal collapse on the surface of the samples was scattered, and the size of the sample microspheres was large, about 6 μm. When the doping amount of Mg^{2+} was gradually increased to 10%, the surface collapse was not significantly improved, and the size of the particles was not much different from that of M0. When the doping amount of Mg^{2+} is greater than 20%, the crystal growth direction on the surface of the microspheres is ordered and tightly bound. The surface of M20 microspheres shows a porous oatmeal shape, and the particle size decreases to 3 μm. The surface of M30 lamellae is upright, dispersed, aggregated, with a good morphology, and shows a dispersed flower structure, and the diameter of the particles is further reduced to about 2 μm. When the doping amount of Mg^{2+} reached 40%, the pore structure on the surface gradually disappeared, and the bonding became tighter, gradually transforming into a dense and smooth spherical structure (M50). From the transmission electron microscopy images (**Figure 2B** and **Additional Figure 2**), it can be seen that when the doping amount of Mg^{2+} is less than 10%, the microsphere surface mostly shows flaky and needle-like HAP assemblies, with disorganised growth directions. When the doping amount of Mg^{2+} is gradually increased, the surface morphology of microspheres is gradually stabilised and tightly bound. The M30 crystal growth direction is highly organised, and the surface deposition is compact and dispersed, reaching a good equilibrium. The surface of M50 tends to be smooth, forming a spherical shape with a compact surface. The size of microspheres in the M30–M50 group is about 2 μm, which is almost one-third of M0. The difference in atomic size leads to lattice distortion, with Mg having smaller atomic sizes than calcium, which can further cause differences in the crystal growth direction, which in turn affects the crystallisation of the material.[33] The smaller particle size helps to achieve a high specific surface area, improve the drug loading efficiency, and facilitate cell phagocytosis to enhance the killing effect on tumour cells. Selected area electron diffraction shows HAP crystal plane streak spacing of 0.344 nm and 0.284 nm, which corresponds to the (002) and (211) crystal planes of the HAP crystal, respectively (**Figure 2C**). Selected area diffraction shows speckled diffraction rings, which is attributed to the good crystallinity and dispersion of Mg particles. **Figure 2D** shows a schematic of Mg^{2+} doped substituted HAP with Mg substitution at CaII sites. Elemental analysis (**Figure 2E**) showed a uniform distribution of Mg and Ca elements in the microspheres (M30). It is worth mentioning that the actual doping ratio of Mg^{2+} should be lower than the stoichiometric ratio during the preparation process because the doping of Mg^{2+} by Ca^{2+} in the hexagonal structure of HAP is limited.[34]

The effect of different Mg^{2+} doping levels on the HAP phase was detected by X-ray diffraction. (**Figure 2F** and **Additional Figure 3**). All samples were identified as HAP by comparison with PDF standard card library (PDF# 09-0432).[35] The characteristic diffraction peaks of HAP doped with different amounts of Mg^{2+} were shifted (**Additional Table 3**), indicating that Mg^{2+} was successfully incorporated into the HAP lattice, which in turn affected the HAP crystallisation (**Additional Table 4**). Theoretically, the incorporation of larger atoms causes the X-ray diffraction peak to shift to the left and *vice versa*.[36, 37] However, the diffraction peaks of (002) and (211) moved in opposite directions, which may be attributed to the presence of macroscopic residual stresses causing lattice distortions affecting the movement of the diffraction peaks. The existence of lattice distortions can be confirmed by further measuring HAP's crystallinity and crystal size in each experimental group. The crystal size of MHA (M1–50) is significantly smaller than that of the M0 group (**Additional Table 4**), which further confirms the successful incorporation of Mg^{2+} in the HAP lattice. Since the size of the Mg atoms is smaller than that of the calcium atoms, the lattice shrinks when the calcium atoms are replaced by the Mg atom, which in turn leads to a reduction in the crystal size.

The Fourier transform infrared spectrometer results (**Figure 2G**) showed that the main characteristic absorption peaks of MHA were the H-O bond (3431 cm^{-1}) and P-O bond (1034 cm^{-1}), which correspond to OH^- and PO_4^{3-} of HAP, respectively. The appearance of characteristic absorption peaks of CO_3^{2-} (1620, 1417, and 876 cm^{-1}) are due to the entry of carbonate ions into the HAP lattice after the decomposition of $CO(NH_2)_2$ during the preparation of MHA. The obtained MHA containing partial CO_3^{2-} is bio-HAP, it is closer to the human bone component and may have better biocompatibility.[38, 39]

The M0 and M10–30 all had IV-type nitrogen adsorption-desorption curves with H3-type hysteresis loops (**Figure 3A**), suggesting that the microspheres have a conical pore structure. The specific surface areas of M10–30 were 177.42, 198.34, and 186.06 m^2/g, respectively, which were significantly higher than those of the un-doped Mg^{2+} (115.50 m^2/g). The pore size distribution curves show that the pore size distribution of MHA is broad, which is due to the macroporous structure of HAP crystals (**Figure 3B** and **C**). In addition, different from other MHA samples, the pore size distribution curve of M30 has a distinct narrow peak at 30–50 nm, which may be due to the mesoporous structure of HAP guided by Mg^{2+} doping, and most of the nanopores of M30 exist in the form of mesopores. With the increase of Mg^{2+} doping, the pore size gradually decreases from the macroporous structure of M0 to the mesoporous structure of M30. In addition, the addition of Mg^{2+} causes lattice distortion of HAP, and the increase in Mg^{2+} content leads to the decrease of MHA particle size and the increase in specific surface area, which helps to improve the loading rate of the subsequent ICA and other drugs. The release of Mg^{2+} leads to the partial collapse of the crystal structure of HAP and breaks the bond between the loaded drug and OH- and other chemical bonding in the HAP, which promotes the release of Ca^{2+} in the HAP and loaded drug, fully utilising the role of drug and Ca^{2+} in bone tissue therapy. According to the crystallinity data (**Additional Table 4**), the crystallinity of M30 was significantly higher than that of M20, and the internal structure of the microspheres was more tightly bound and ordered, which is expected to achieve long-term slow release of the drug under the weak acidic environment *in vivo* and contribute to the long-term repair of bone tissue. Based

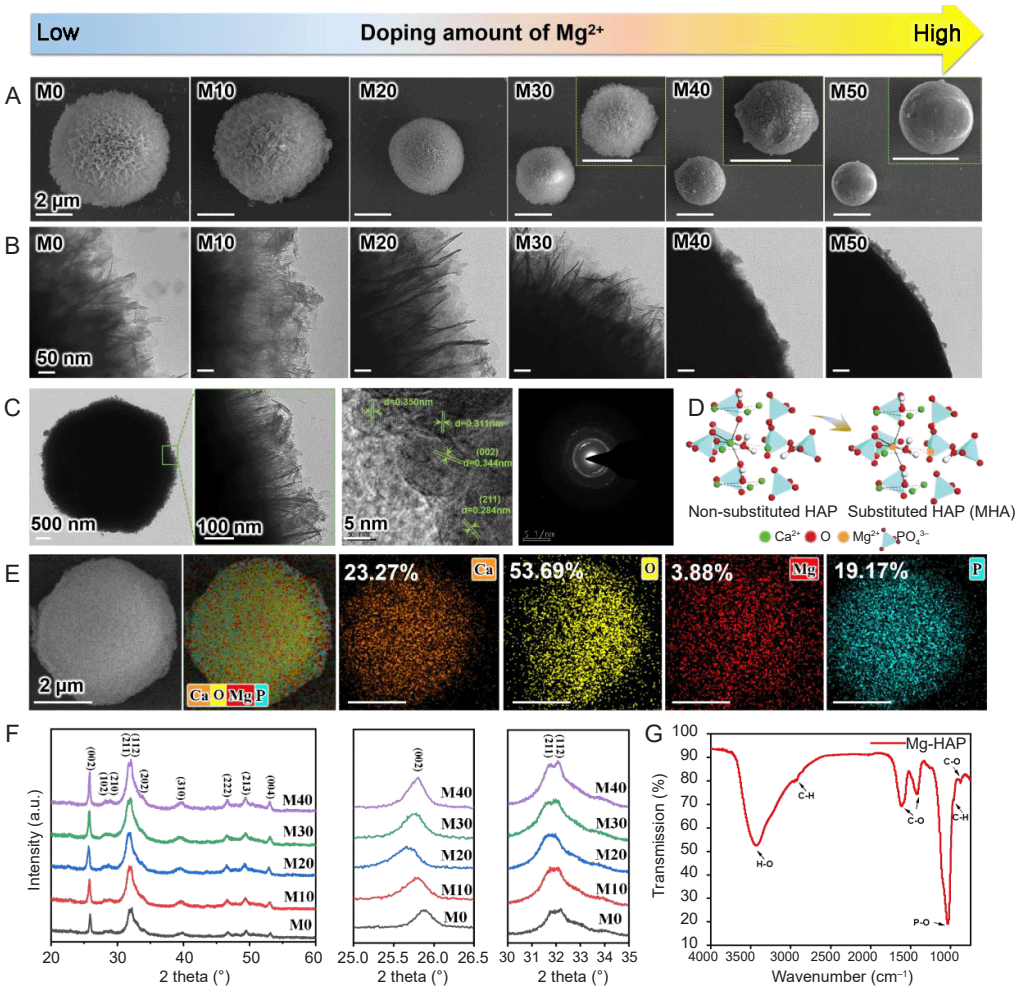

Figure 2. (A) The SEM images of M0–50. (B, C) The TEM images of M0–50. (D) Schematic diagram of Mg-doped HAP. Created with Adobe Photoshop and Microsoft PowerPoint 2021. (E) Elemental distribution of M30. Scale bars: 2 μm (A, E), 50 nm (B), 500 nm, 100 nm and 5 nm (C). (F) X-ray diffraction pattern of MHA with different Mg-doped content. (G) Fourier transform infrared spectrometer of M30. a.u.: arbitrary unit; M0–50: the addition of Mg^{2+} (Mg^{2+}/Mg^{2+} + Ca^{2+}) × 100%) was 0–50% in the MHA; Mg: magnesium; MHA: Mg^{2+}-doped abalone shell-derived mesoporous hydroxyapatite microspheres; SEM: scanning electron microscopy; TEM: transmission electron microscopy.

on the above observations and analysis, the M30 samples had good surface morphology, orderly crystal growth, high crystallinity, small microsphere size, mesoporous structure with high specific surface area, which could help to achieve high drug loading and release, and could realise the long-term and efficient therapeutic effect of MHA microspheres, so the M30 samples were selected for subsequent experiments and analyses.

The ion release results of Mg-HAP (**Figure 3D**) showed that Mg^{2+} and Ca^{2+} were released slowly within 28 days, indicating their good stability and controlled sustained release properties. Initially, it released Mg^{2+} and Ca^{2+} at a faster rate due to its large spherical mesoporous pore channel. With the degradation of microspheres, the spherical size decreased gradually, resulting in a slower release rate of elements. Interestingly, the content of Mg was much higher than that of Ca in the inductively coupled plasma analysis while Mg content was lower than Ca in the energy dispersive spectroscopy energy spectrum test. This is mainly due to the distortion of some HAP lattice caused by the doping of Mg, and thus this part of HAP is easier to decompose and then release Mg^{2+}, while the HAP with no lattice distortion is structurally stable, and decomposes slowly, and thus has a lower concentration of Ca^{2+}. The high concentration of P in the figure is due to the high concentration of P in the PBS. The long-term release of Mg and Ca elements is conducive to promoting bone repair and tumour control and achieving more efficient therapeutic effects.

Drug-loading ability and ICA release behaviour *in vitro*

By combining the standard curve (**Additional Figure 4**) and the absorbance of the supernatant measured during the preparation of the drug-carrying microspheres, the loading and encapsulation rates of MHA were calculated to be 7.69% and 83.29%, respectively, showing a high drug loading effect. It was attributed to its large specific surface area, which could provide more OH^- to form hydrogen bonds with ICA. The IMHA microspheres released ICA continuously over 60 hours at different pH values and exhibited a controlled sustained release, which was related to their conical mesoporous structure (**Figure 3E**). In the first 10 hours, ICA adsorbed on

the surface of the microsphere was first released due to the breakage of hydrogen bonds. As time passed, the microsphere began to degrade and loosen, and the drug stored in the mesoporous channels started to release (**Figure 3F**). Due to the conical structure of the mesoporous channels, less drug was stored in the mesoporous channel, so the drug release rate decreased. In addition, based on the weakly acidic microenvironment around the tumour, the cumulative drug release was measured at different pH values (pH 6.4 > pH 5.6 > pH 7.4), and the results demonstrated that IMHA was significantly pH-responsive and pH-selective (**Figure 3E**). A series of studies revealed that HAP has stability differences at different pH values.[9,40] When IMHA is in acidic condition, the environment contains a large amount of H^+, which preferentially binds to OH^- on the surface of HAP and destroys the hydrogen bond formed between OH^- and ICA. H^+ competes with ICA for the active site, resulting in a large amount of ICA release. However, when the acidity is too strong, it may lead to a change in HAP structural stability, which affects the activity of IMHA surface sites, and ultimately leads to a decrease in ICA release (pH 6.4 > pH 5.6). The results showed that IMHA was released in the highest amount under weakly acidic (pH = 6.4) conditions. It is noteworthy that the pH selectivity of IMHA30 makes it well-suited as an anti-tumour drug delivery system due to the weakly acidic microenvironment surrounding tumours.[41]

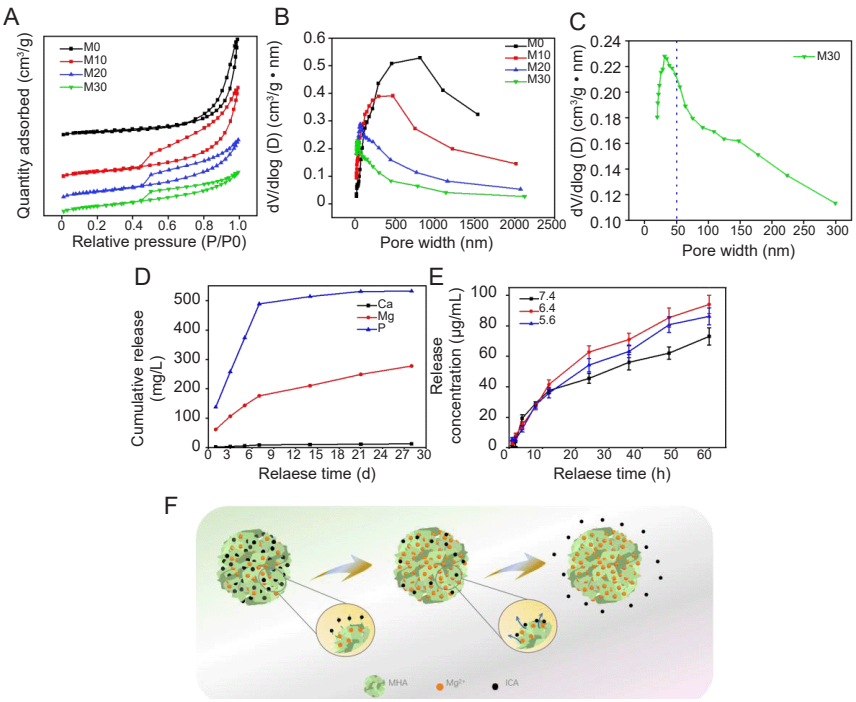

Figure 3. (A) Nitrogen adsorption-desorption curve of M0–30. (B, C) The pore size distribution curve of M30. A dashed line is marked at 50 nm, which is the maximum pore size of the mesoporous structure. (D) The inductively coupled plasma analysis of M30. (E) ICA release concentrations of of M30 at different pH (pH = 5.6, 6.4, and 7.4). (F) Schematic diagram of ICA release from IMHA. Created by Microsoft Office PowerPoint 2019 and Adobe Photoshop 2022 software. The pore size of 2–50 nm is defined as mesoporous structure. ICA: icariin; M0–30: The addition of Mg^{2+} ($Mg^{2+}/Mg^{2+} + Ca^{2+}$) × 100%) was 0–30% in the MHA; MHA: Mg^{2+}-doped abalone shell-derived mesoporous hydroxyapatite microspheres.

The *in vitro* biocompatibility of MHA and IMHA

Figure 4A and **B** show the haemolysis test results of IMHA mixed with red blood cells of New Zealand white rabbits at different concentrations. Optical photographs showed that there was obvious colour stratification occurred in the experimental and negative control groups at all concentrations, and the supernatant was clear and transparent (**Figure 4B**). The haemolysis rate of IMHA at all concentrations was less than 5% (**Figure 4A**), and no haemolysis phenomenon occurred, indicating good biocompatibility of the microspheres.

The biocompatibility of MHA and IMHA were evaluated by co-culturing with BMSCs (**Figure 4C1**). BMSCs were co-cultured with unloaded drug-loaded MHA for 3 days and the cell viability were calculated on days 1, 2, and 3, respectively. At lower MHA concentrations (50–100 μg/mL), cells continued to proliferate compared to the control. When the MHA concentration was up to 1000 μg/mL, a decrease in cell viability was clearly observed. This indicates that a certain concentration of MHA can promote the proliferation of BMSCs, while an excess affects the growth of cells. Thereafter, BMSCs were co-cultured with IMHA, and the cell growth viability of the experimental groups at all concentrations was significantly higher than that of the control group (**Figure 4C2**), indicating that they both promoted the proliferation of BMSCs. Among them, the highest cell viability rate was observed at the concentrations of 100 and 500 μg/mL. The

results indicated that MHA had good biocompatibility before and after drug loading at suitable concentrations and exerted its carrier properties and functions.

Inhibition and ablation of MG63 osteosarcoma cells *in vitro*

To explore the anti-tumour effect of microspheres, MHA and IMHA were co-cultured with MG63 cells respectively, and then AO/EB fluorescence staining and CCK-8 detection were performed (**Figure 4D** and **E**). Compared with the control group, it can be considered that there is little difference in the OD value of MHA at all concentrations. However, the OD values for each concentration of IMHA were significantly lower than those of the control. When the concentration of IMHA reached 500 μg/mL, its OD value decreased significantly, indicating a dramatic decrease in the number of viable cells. According to the more intuitive results of AO/EB staining, after 3 days of co-culture with different concentrations of MHA, the growth number of MG63 cells was similar, and the number of cells decreased under the conditions of 500 and 1000 mg/L MHA, and some cells were spherical, which indicated that MHA environment was not suitable for the growth of MG63 cells. After 3 days of co-culture with IMHA, compared with the control group, when the concentration of IMHA was 50 and 100 mg/L, the number of living cells decreased and the cell growth density decreased significantly. When the concentration of IMHA reached 500 and 1000 mg/L, a large number of orange-red or orange-yellow abnormal dead cells were observed, and the number of damaged and apoptotic cells increased sharply, which further explained the apoptosis-inducing effect of IMHA on MG63 cells, which was consistent with the experimental results of CCK-8. By comparison, we can see that ICA has a high-efficiency damage effect on MG63 osteosarcoma cells. This indicates that IMHA after loading ICA has a good inhibitory effect on MG63 osteosarcoma cells and can effectively induce the osteosarcoma cell death.[42]

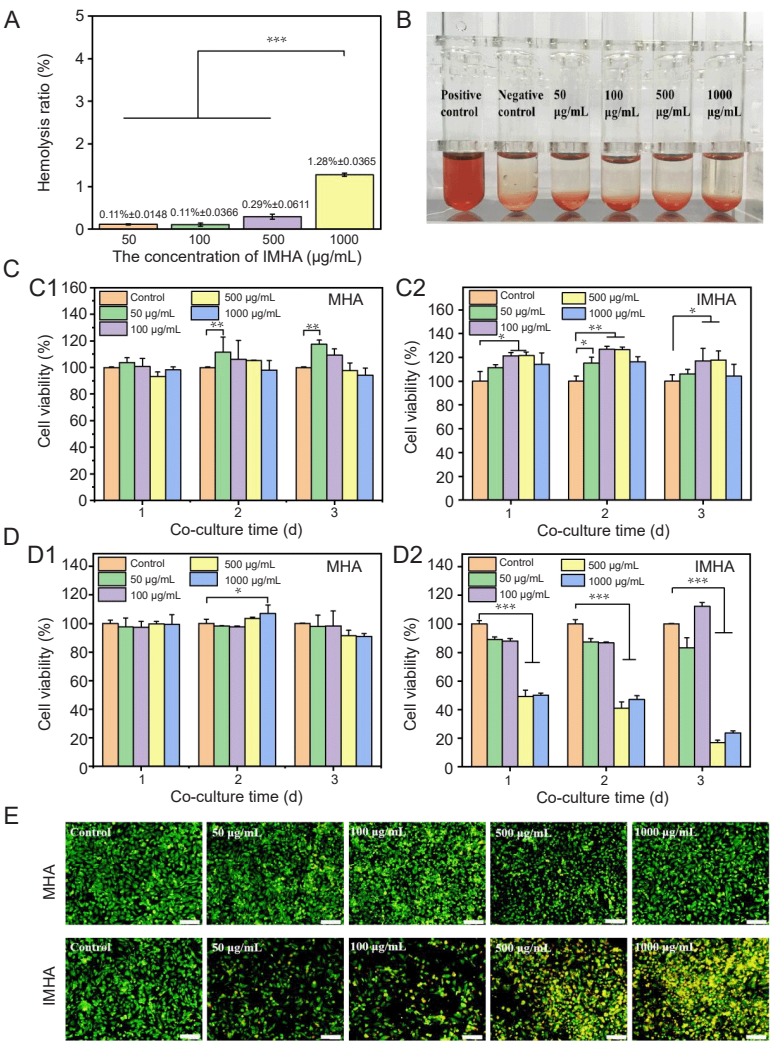

Figure 4. (A, B) The haemolysis ratio (A) and appearance (B) of IMHA. (C) CCK-8 cytotoxicity analysis of BMSCs cultured with MHA and IMHA. (D, E) CCK-8 cytotoxicity analysis (D) and AO/EB staining (E) of MG63 cells cultured with MHA and IMHA on the 3rd day. Scale bars: 200 μm. All data are expressed as the mean ± SD. $^{*}P < 0.05$, $^{**}P < 0.01$, $^{***}P < 0.001$ (one-way analysis of variance followed by least significant difference *post hoc* test). AO: acridine orange; BMSC: bone marrow mesenchymal stem cell; CCK-8: Cell Counting Kit-8; EB: ethidium bromide; IMHA: Mg^{2+}/icariin smart dual delivery system; MHA: Mg^{2+}-doped abalone shell-derived mesoporous hydroxyapatite microspheres.

Exploration of anti-tumour mechanism

To further explore the inhibitory mechanism of MG63 osteosarcoma cells, the double-cell apoptosis, cell cycle, and gene expression of IMHA were detected. Annexin V-FITC assay results showed that the number of normal cells decreased from 95.1% to 52.4% with increasing IMHA co-culture concentration, while the number of early and late apoptotic cells significantly increased from 1.50% and 2.17% to 38.6% and 6.69%, respectively (**Figure 5A**). This indicates that IMHA can induce apoptosis, which is gradually enhanced with increasing of IMHA concentration. A large number of dead cells in cytotoxicity analysis are also the result of apoptosis.[43, 44]

For a more in-depth study of the causes of apoptosis, cell cycle assays were performed (**Figure 5B**). The G1 peak of MG63 cells in the blank group was higher (71.7%), while that in the G2 phase was lower (17.7%). MG63 cells treated with IMHA showed a dose-dependent increase in the G2 phase. When the concentration of IMHA reached 1000 μg/mL, the peak of the G1 phase decreased to 40.1%, while the peaks of the G2 phase increased to 42.5%, indicating that the molecular target of IMHA promoting apoptosis of osteosarcoma cells was the G2 phase, thus affecting cell proliferation and DNA replication.[45]

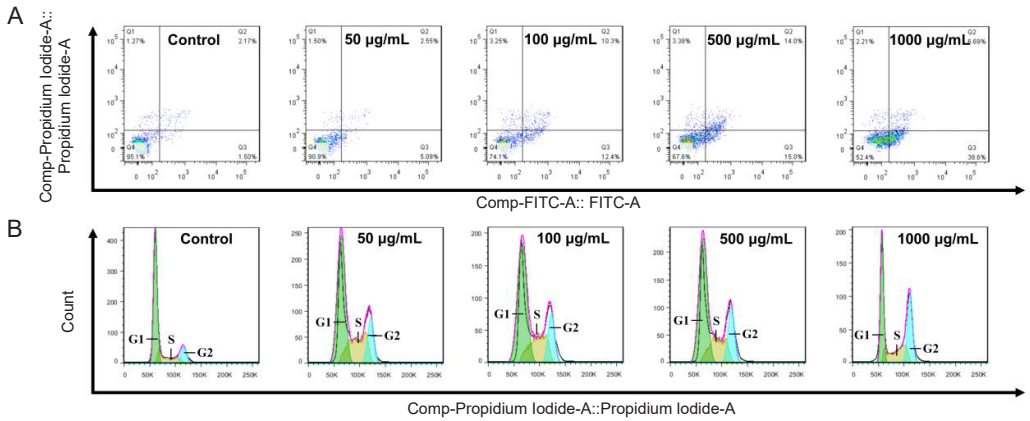

Figure 5. (A, B) The cell apoptosis (A) and cycle distribution (B) of MG63 cells cultured with different concentrations of IMHA. FITC: Fluorescein Isothiocyanate.

As shown by the detection of the expression of some apoptotic genes in MG63 cells (**Figure 6A**), different concentrations of IMHA effectively promoted the high expression of four apoptotic genes (*Bcl-2*, *caspase-3*, *caspase-8* and *caspase-9*). 100 μg/mL of IMHA was slightly less effective on *Bcl-2*, *caspase-3*, and *caspase-8* than the other three concentrations. However, the high expression was most obvious when the concentration reached 1000 μg/mL, and the expression of the four apoptotic genes was significantly higher than that of 50, 100 and 500 μg/mL. It is also worth noting that the prominent expression of *caspase-3* and *caspase-8* apoptotic genes was higher than 100 μg/mL at an IMHA concentration of 50 μg/mL, which may be based on the selectivity of the drug on the expression of apoptotic genes as well as the result of the complex regulation of the gene expression pathway. It can be proved that IMHA can effectively promote the transformation of MG63 cells to G2 phase and inhibit cell proliferation. In addition, IMHA achieved apoptosis induction by regulating the expression of four apoptotic genes, *Bcl-2*, *caspase-3*, *caspase-8* and *caspase-9* (**Figure 6B**). Therefore, the good biocompatibility, Mg^{2+}/ICA smart dual delivery and anti-tumour properties of HAP endow it with potential applications in drug delivery and tumour therapy.

Discussion

Abalone shells with high calcium content were successfully converted into Mg-doped HAP mesoporous microspheres using hydrothermal synthesis for application as an Mg^{2+}/ICA intelligent dual drug delivery system. The doping of Mg element reduces the size of the HAP mesoporous microsphere and increases their specific surface area, thereby improving their drug-loading efficiency.

The MHA mesoporous microspheres can achieve long-term stable release of Mg^{2+} and Ca^{2+} to promote bone repair and tumour control. When MHA was employed as a drug-loading vehicle to load ICA for the treatment of osteosarcoma, IMHA had excellent controlled-release properties and pH selectivity, facilitating drug release in the weakly acidic environment of the tumour. In addition, IMHA can effectively promote the proliferation of BMSCs and induce the high expression of apoptotic genes (*Bcl-2*, *caspase-3*, *caspase-8* and *caspase-9*) in MG63 cells, simultaneously demonstrating that the material is not cytotoxic. Based on the dual action of IMHA on both BMSCs and MG63 cells, it is expected to achieve efficient treatment of bone cancer and other diseases. However, the more intuitive toxicity test, animal application, *in vivo* and *ex vivo* induction mechanism, pathway of action and gene regulation of IMHA have not been clarified yet, and need to be further explored and improved in the future.

Therefore, the combination of superior properties such as good biocompatibility, controlled sustained drug release and anti-tumour activity endows IMHA with potential clinical applications in drug delivery and tumour therapy.

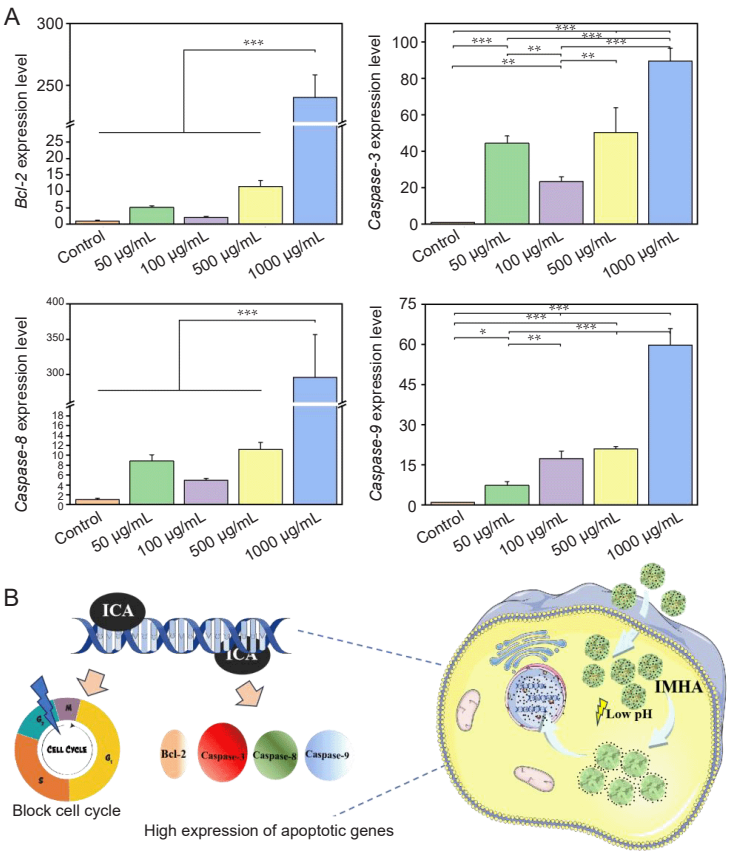

Figure 6. Expression levels of apoptotic genes (A) and mechanism of action (B) in MG63 cells at different concentrations of IMHA. B was created with Adobe Photoshop and Microsoft PowerPoint 2021. All data are expressed as the mean ± SD. $*P < 0.05$, $**P < 0.01$, $***P < 0.001$ (one-way analysis of variance followed by least significant difference *post hoc* test). ICA: icariin; IMHA: Mg^{2+}/icariin smart dual delivery system.

Author contributions

JC: conceptualization, project administration, funding acquisition; JC, PP: project administration, funding acquisition; SZ, DT: investigation. KL, MC, HY: methodology; KL, MC, HH: data curation; KL, JZ: formal analysis, KL, MC: writing - original draft; MC: visualization; JC, HH: resources; HY: validation; JW, PP, JC: supervision; PP: writing - review & editing. All authors approved the final version of the manuscript.

Financial support

This study was supported by Open Foundation of State Key Laboratory of Mineral Processing (No. BGRIMM-KJSKL-2023-23), Shandong Laboratory of Advanced Materials and Green Manufacturing (No. AMGM2021F02), Natural Science Foundation of Shandong Province (Nos. ZR2022QD057, ZR2023MC125), Open Project Fund for Hubei Key Laboratory of Oral and Maxillofacial Development and Regeneration (No. 2021kqhm003), and China Postdoctoral Science Foundation (Nos. 2022M722434, 2023T160492).

Acknowledgement

We thank the supported from by Physical-Chemical Materials Analytical & Testing Center of Shandong University at Weihai on physical, chemical, and characterization performance testing equipment and related technical support.

Conflicts of interest statement

The authors declare that they have no known competing financial interests or personal relationships that could have appeared to influence the work reported in this paper.

Additional files

Additional file 1: Characterisation of MHA.

Additional Table 1: Raw material consumption in M0–50 sample.

Additional Table 2: The primer sequences of each gene.

Additional Table 3: The 2θ diffraction angles of (002) and (211) lattice planes of MHA.

Additional Table 4: Crystallinity and crystallite size of MHA with different doping dose.

Additional Figure 1: The SEM pattern of MHA with different Mg-doped content.

Additional Figure 2: The TEM pattern of MHA with different Mg-doped content.

Additional Figure 3: Hydroxylapatite (09-0432) PDF Standard Card Library.

Additional Figure 4: The standard curve of ICA.

1. Mushtaq, A.; Zhang, H.; Cui, M.; Lin, X.; Huang, S.; Tang, Z.; Hou, Y.; Zubair Iqbal, M.; Kong, X. ROS-responsive chlorin e6 and silk fibroin loaded ultrathin magnetic hydroxyapatite nanorods for T1-magnetic resonance imaging guided photodynamic therapy in vitro. Colloids Surf Physicochem *Eng Aspects*. **2023**, *656*, 130513.
2. Ribeiro, J. P.; Domingues, R. M. A.; Babo, P. S.; Nogueira, L. P.; Reseland, J. E.; Reis, R. L.; Gomez-Florit, M.; Gomes, M. E. Highly elastic and bioactive bone biomimetic scaffolds based on platelet lysate and biomineralized cellulose nanocrystals. *Carbohydr Polym*. **2022**, *292*, 119638.
3. Wang, G.; Lv, Z.; Wang, T.; Hu, T.; Bian, Y.; Yang, Y.; Liang, R.; Tan, C.; Weng, X. Surface functionalization of hydroxyapatite scaffolds with MgAlEu-LDH nanosheets for high-performance bone regeneration. *Adv Sci (Weinh)*. **2022**, *10*, e2204234.

4. Cheng, M.; Liu, M.; Chang, L.; Liu, Q.; Wang, C.; Hu, L.; Zhang, Z.; Ding, W.; Chen, L.; Guo, S.; Qi, Z.; Pan, P.; Chen, J. Overview of structure, function and integrated utilization of marine shell. S*ci Total Environ.* **2023**, *870*, 161950.
5. Huang, H.; Du, M.; Chen, J.; Zhong, S.; Wang, J. Preparation and characterization of abalone shells derived biological mesoporous hydroxyapatite microspheres for drug delivery. *Mater Sci Eng C Mater Biol Appl.* **2020**, *113*, 110969.
6. Pan, P.; Geng, Y.; Hu, L.; Liu, Q.; Liu, M.; Cheng, M.; Chen, L.; Chen, J. Biologically enhanced 3D printed micro-nano hybrid scaffolds doped with abalone shell for bone regeneration. *Adv Compos Hybrid Mater.* **2022**, *6*, 10.
7. Karunakaran, G.; Cho, E. B.; Kumar, G. S.; Kolesnikov, E.; Sudha, K. G.; Mariyappan, K.; Han, A.; Choi, S. S. Citric acid-mediated microwave-hydrothermal synthesis of mesoporous f-doped HAp nanorods from bio-waste for biocidal implant applications. *Nanomaterials (Basel).* **2022**, *12*, 315.
8. Qi, Y.; Qian, Z.; Yuan, W.; Li, Z. Injectable and self-healing nanocomposite hydrogel loading needle-like nano-hydroxyapatite and graphene oxide for synergistic tumour proliferation inhibition and photothermal therapy. *J Mater Chem B.* **2021**, *9*, 9734-9743.
9. Wen, Z.; Wang, Z.; Chen, J.; Zhong, S.; Hu, Y.; Wang, J.; Zhang, Q. Manipulation of partially oriented hydroxyapatite building blocks to form flowerlike bundles without acid-base regulation. *Colloids Surf B Biointerfaces.* **2016**, *142*, 74-80.
10. Ma, Q.; Liao, J.; Tian, T.; Zhang, Q.; Cai, X. A potential flower-like coating consisting of calcium-phosphate nanosheets on titanium surface. *Chin Chem Lett.* **2017**, *28*, 1893-1896.
11. Munir, M. U.; Salman, S.; Javed, I.; Bukhari, S. N. A.; Ahmad, N.; Shad, N. A.; Aziz, F. Nano-hydroxyapatite as a delivery system: overview and advancements. *Artif Cells Nanomed Biotechnol.* **2021**, *49*, 717-727.
12. Pan, P.; Yue, Q.; Li, J.; Gao, M.; Yang, X.; Ren, Y.; Cheng, X.; Cui, P.; Deng, Y. Smart cargo delivery system based on mesoporous nanoparticles for bone disease diagnosis and treatment. *Adv Sci (Weinh).* **2021**, *8*, e2004586.
13. Doan, V. H. M.; Mondal, S.; Vo, T. M. T.; Ly, C. D.; Vu, D. D.; Nguyen, V. T.; Park, S.; Choi, J.; Oh, J. Fluorescence conjugated nanostructured cobalt-doped hydroxyapatite platform for imaging-guided drug delivery application. *Colloids Surf B Biointerfaces.* **2022**, *214*, 112458.
14. Nenen, A.; Maureira, M.; Neira, M.; Orellana, S. L.; Covarrubias, C.; Moreno-Villoslada, I. Synthesis of antibacterial silver and zinc doped nano-hydroxyapatite with potential in bone tissue engineering applications. *Ceram Int.* **2022**, *48*, 34750-34759.
15. Słota, D.; Florkiewicz, W.; Piętak, K.; Pluta, K.; Sadlik, J.; Miernik, K.; Sobczak-Kupiec, A. Preparation of PVP and betaine biomaterials enriched with hydroxyapatite and its evaluation as a drug carrier for controlled release of clindamycin. *Ceram Int.* **2022**, *48*, 35467-35473.
16. Govindan, B.; Swarna Latha, B.; Nagamony, P.; Ahmed, F.; Saifi, M. A.; Harrath, A. H.; Alwasel, S.; Mansour, L.; Alsharaeh, E. H. Designed synthesis of nanostructured magnetic hydroxyapatite based drug nanocarrier for anti-cancer drug delivery toward the treatment of human epidermoid carcinoma. *Nanomaterials (Basel).* **2017**, *7*, 138.
17. Karunakaran, G.; Cho, E. B.; Kumar, G. S.; Kolesnikov, E.; Karpenkov, D. Y.; Gopinathan, J.; Pillai, M. M.; Selvakumar, R.; Boobalan, S.; Gorshenkov, M. V. Sodium dodecyl sulfate mediated microwave synthesis of biocompatible superparamagnetic mesoporous hydroxyapatite nanoparticles using black Chlamys varia seashell as a calcium source for biomedical applications. *Ceram Int.* **2019**, *45*, 15143-15155.
18. Franco, D.; Calabrese, G.; Petralia, S.; Neri, G.; Corsaro, C.; Forte, L.; Squarzoni, S.; Guglielmino, S.; Traina, F.; Fazio, E.; Conoci, S. Antimicrobial effect and cytotoxic evaluation of Mg-doped hydroxyapatite functionalized with Au-nano rods. *Molecules.* **2021**, *26*, 1099.
19. Jiang, Z.; Gong, Z.; Song, W.; Wu, P.; Deng, C.; Chen, Q.; Yan, T. A promising hydroxyapatite whisker with long-term and high-efficiency antibacterial performance and its potential application in implant. *Inorg Chem Commun.* **2022**, *146*, 109860.
20. Martínez-Gracida, N. O.; Esparza-González, S. C.; Castillo-Martínez, N. A.; Serrano-Medina, A.; Olivas-Armendariz, I.; Campos-Múzquiz, L. G.; Múzquiz-Ramos, E. M. Synergism in novel silver-copper/hydroxyapatite composites for increased antibacterial activity and biocompatibility. *Ceram Int.* **2020**, *46*, 20215-20225.
21. Wei, J. Q.; Liu, Y.; Zhang, X. H.; Liang, W. W.; Zhou, T. F.; Zhang, H.; Deng, X. L. Enhanced critical-sized bone defect repair efficiency by combining deproteinized antler cancellous bone and autologous BMSCs. *Chin Chem Lett.* **2017**, *28*, 845-850.
22. Hou, H. H.; Lee, B. S.; Liu, Y. C.; Wang, Y. P.; Kuo, W. T.; Chen, I. H.; He, A. C.; Lai, C. H.; Tung, K. L.; Chen, Y. W. Vapor-induced pore-forming atmospheric-plasma-sprayed zinc-, strontium-, and magnesium-doped hydroxyapatite coatings on titanium implants enhance new bone formation-an in vivo and in vitro investigation. *Int J Mol Sci.* **2023**, *24*, 4933.
23. Yu, S.; Sun, T.; Liu, W.; Yang, L.; Gong, H.; Chen, X.; Li, J.; Weng, J. PLGA cage-like structures loaded with Sr/Mg-doped hydroxyapatite for repairing osteoporotic bone defects. *Macromol Biosci.* **2022**, *22*, e2200092.
24. Paramasivan, M.; Sampath Kumar, T. S.; Kanniyappan, H.; Muthuvijayan, V.; Chandra, T. S. Biomimetic ion substituted and Co-substituted hydroxyapatite nanoparticle synthesis using Serratia Marcescens. *Sci Rep.* **2023**, *13*, 4513.
25. Tithito, T.; Sillapaprayoon, S.; Pimtong, W.; Thongbunchoo, J.; Charoenphandhu, N.; Krishnamra, N.; Lert-Itthiporn, A.; Maneeprakorn, W.; Pon-On, W. Development of biomaterials based on biomimetic trace elements co-doped hydroxyapatite: physical, in vitro osteoblast-like cell growth and in vivo cytotoxicity in zebrafish studies. *Nanomaterials (Basel).* **2023**, *13*, 255.
26. Pan, P.; Yue, Q.; Yang, X.; Ren, Y.; Alharthi, F. A.; Alghamdi, A.; Su, J.; Deng, Y. Structure engineering of yolk-shell magnetic mesoporous silica microspheres with broccoli-like morphology for efficient catalysis and enhanced cellular uptake. *Small.* **2021**, *17*, e2006925.
27. Yu, L.; Pan, P.; Yu, B.; Yang, X.; Yue, Q.; Alghamdi, A. A.; Ren, Y.; Deng, Y. Interface assembly to magnetic mesoporous organosilica microspheres with tunable surface roughness as advanced catalyst carriers and adsorbents. *ACS Appl Mater Interfaces.* **2021**, *13*, 36138-36146.
28. Weng, R.; Zhang, L.; Cao, Y.; Wang, Z.; Zhao, C.; Wang, J.; Zhao, C. Two-dimensional borocarbonitrides nanosheets engineered sulfonated polyether sulfone microspheres as highly efficient and photothermally recyclable adsorbents for hemoperfusion. *Chem Eng J.* **2023**, *463*, 142365.
29. Zhong, R.; Zhong, Q.; Huo, M.; Yang, B.; Li, H. Preparation of biocompatible nano-ZnO/chitosan microspheres with multi-functions of antibacterial, UV-shielding and dye photodegradation. *Int J Biol Macromol.* **2020**, *146*, 939-945.
30. Yang, Y.; Qiao, X.; Huang, R.; Chen, H.; Shi, X.; Wang, J.; Tan, W.; Tan, Z. E-jet 3D printed drug delivery implants to inhibit growth and

metastasis of orthotopic breast cancer. *Biomaterials.* **2020**, *230*, 119618.

31. Xuerong, Z.; Ao, S.; Jianping, W.; Xin, Z.; Duoduo, T.; Mingjuan, W.; Lijun, X.; Enhong, Z.; Cui, Z. G. Effects of long noncoding RNA AK093407 on the biological behavior of colon cancer cells and the underlying mechanism. *Comb Chem High Throughput Screen.* **2023**, *26*, 289-300.
32. Zhang, J.; Cui, J.; Wang, Y.; Lin, X.; Teng, X.; Tang, Y. Complex molecular mechanism of ammonia-induced apoptosis in chicken peripheral blood lymphocytes: miR-27b-3p, heat shock proteins, immunosuppression, death receptor pathway, and mitochondrial pathway. *Ecotoxicol Environ Saf.* **2022**, *236*, 113471.
33. Zhang, J.; Tang, L.; Qi, H.; Zhao, Q.; Liu, Y.; Zhang, Y. Dual function of magnesium in bone biomineralization. *Adv Healthc Mater.* **2019**, *8*, e1901030.
34. Zhao, Z.; Espanol, M.; Guillem-Marti, J.; Kempf, D.; Diez-Escudero, A.; Ginebra, M. P. Ion-doping as a strategy to modulate hydroxyapatite nanoparticle internalization. *Nanoscale.* **2016**, *8*, 1595-1607.
35. de Wolff, P. Technisch Physische Dienst. Delft, The Netherlands,1957.
36. Pagan, D. C.; Shade, P. A.; Barton, N. R.; Park, J. S.; Kenesei, P.; Menasche, D. B.; Bernier, J. V. Modeling slip system strength evolution in Ti-7Al informed by in-situ grain stress measurements. *Acta Mater.* **2017**, *128*, 406-417.
37. Vlasic, T. M.; Servio, P. D.; Rey, A. D. Effect of guest size on the mechanical properties and molecular structure of gas hydrates from first-principles. *Cryst Growth Des.* **2017**, *17*, 6407-6416.
38. Teruel Jde, D.; Alcolea, A.; Hernández, A.; Ruiz, A. J. Comparison of chemical composition of enamel and dentine in human, bovine, porcine and ovine teeth. *Arch Oral Biol.* **2015**, *60*, 768-775.
39. Sanosh, K. P.; Chu, M. C.; Balakrishnan, A.; Lee, Y. J.; Kim, T. N.; Cho, S. J. Synthesis of nano hydroxyapatite powder that simulate teeth particle morphology and composition. *Curr Appl Phys.* **2009**, *9*, 1459-1462.
40. Sharma, R.; Pandey, R. R.; Gupta, A. A.; Kar, S.; Dhayal, M. In situ amino acid functionalization and microstructure formation of hydroxyapatite nanoparticles synthesized at different pH by precipitation route. *Mater Chem Phys.* **2012**, *133*, 718-725.
41. Mi, P.; Kokuryo, D.; Cabral, H.; Wu, H.; Terada, Y.; Saga, T.; Aoki, I.; Nishiyama, N.; Kataoka, K. A pH-activatable nanoparticle with signal-amplification capabilities for non-invasive imaging of tumour malignancy. *Nat Nanotechnol.* **2016**, *11*, 724-730.
42. Ren, H.H.; Zhao, H. Y.; Cui, Y.; Ao, X.; Li, A. L.; Zhang, Z. M.; Qiu, D. Poly(1,8-octanediol citrate)/bioactive glass composite with improved mechanical performance and bioactivity for bone regeneration. *Chin Chem Lett.* **2017**, *28*, 2116-2120.
43. Bhattacharjee, A.; Bose, S. Multifunctional polydopamine - Zn(2+)-curcumin coated additively manufactured ceramic bone grafts with enhanced biological properties. *Biomater Adv.* **2023**, *153*, 213487.
44. Marinho, J. P. N.; Neme, N. P.; Matos, M. J. d. S.; Batista, R. J. C.; Macedo, W. A. d. A.; Gastelois, P. L.; Gomes, D. A.; Rodrigues, M. A.; Cipreste, M. F.; Sousa, E. M. B. d. Nanostructured system based on hydroxyapatite and curcumin: a promising candidate for osteosarcoma therapy. *Ceram Int.* **2023**, *49*, 19932-19949.
45. Yuan, P.; Min, Y.; Zhao, Z. Multifunctional nanoparticles for the treatment and diagnosis of osteosarcoma. *Biomater Adv.* **2023**, *151*, 213466.

Received: February 1, 2024
Revised: February 27, 2024
Accepted: May 24, 2024
Available online: June 28, 2024